



# Isolines in 3D Radar Images for Remote Sensing Applications

Dominique Henry, Hervé Aubert

## ► To cite this version:

Dominique Henry, Hervé Aubert. Isolines in 3D Radar Images for Remote Sensing Applications. 2019 16th European Radar Conference (EuRAD), Oct 2019, Paris, France. hal-03749987

HAL Id: hal-03749987

<https://hal.science/hal-03749987>

Submitted on 11 Aug 2022

**HAL** is a multi-disciplinary open access archive for the deposit and dissemination of scientific research documents, whether they are published or not. The documents may come from teaching and research institutions in France or abroad, or from public or private research centers.

L'archive ouverte pluridisciplinaire **HAL**, est destinée au dépôt et à la diffusion de documents scientifiques de niveau recherche, publiés ou non, émanant des établissements d'enseignement et de recherche français ou étrangers, des laboratoires publics ou privés.

# Isolines in 3D Radar Images for Remote Sensing Applications

Dominique Henry<sup>#1</sup>, Hervé Aubert<sup>#2</sup>

<sup>#</sup>LAAS-CNRS, France

{<sup>1</sup>dhenry, <sup>2</sup>haubert}@laas.fr

**Abstract** — This paper reports a new technique for detecting and remotely analysing electromagnetic scatterers embedded in a scene from 3D radar images. It consists of segmenting the images with *isolines*. An isoline refers to a line along which the radar echo amplitude is the same. A segmentation algorithm based on isolines is proposed here for ensuring that each isoline encloses a unique scatterer. Applications of isolines to precision agriculture are reported.

**Keywords** — radar imaging, electromagnetic scatterers, segmentation, precision agriculture, proximal sensor.

## I. INTRODUCTION

We observe for a decade the increasing development of easy to use FM-CW (Frequency-Modulated Continuous-Wave) millimetre-wave (mm-wave) radars. At first reserved for automotive applications at 77GHz, these radars are now commercialized for industrial applications in ISM bands [1]. Their high frequencies of operation allow designing large modulation bandwidths [2], but also compact antennas for integrated MIMO (Multiple Inputs Multiple Outputs) front-ends [3]. High depth resolutions and fast 3D radar imaging are consequently achieved, paving the way to new remote sensing applications. The aerial radar imaging is then viewed differently, since millimetre-wave radars can now be integrated into UAVs (Unmanned Aerial Vehicles) [4], and not only in aircrafts. Commercially available mm-wave radars offer new opportunities, such as the intra-parcel radar imaging in precision viticulture [5]. If not embedded on vehicles, these systems are ground-based and can be used for SHM (Structural Health Monitoring) [6] or other miscellaneous applications, such as the monitoring of livestock [7].

In many cases, the end-user of mm-wave radars has to deal with a multidimensional data gathered from the illuminated scene. The radar data can be viewed as the spatial and/or time representation of the electromagnetic backscattering from the scene. In this paper, we propose a new technique for segmenting and remote analysing 3D radar images. It consists of segmenting the images with *isolines* or iso-echo lines. An isoline refers to a line along which the radar echo amplitude is the same. A segmentation algorithm is proposed for ensuring that each isoline encloses a unique scatterer. This generic technique is illustrated here in the framework of two different practical applications: (i) the remote estimation of the vine grape yield at 24GHz, 77GHz and 122GHz, and (ii) the monitoring of apple trees and vine plants seasonal development.

## II. NOVEL SEGMENTATION TECHNIQUE OF 3D RADAR IMAGE

### A. Spatial resolution of 3D radar image

First, we consider a FM-CW radar transmitting a chirp with a carrier frequency  $f_c$  and modulation bandwidth  $B$ . The theoretical depth resolution  $d$  is then given by  $= c/2B$ , where  $c$  denotes the velocity of light. A beamscanning is performed in order to obtain the electromagnetic signal backscattered by the illuminated scene in the given direction  $(\theta, \varphi)$ , where  $\theta$  and  $\varphi$  designate the direction in elevation and azimuth, respectively. Depending on the front-end configuration of the radar, the beamscanning might be electrical or mechanical. The scene is viewed as a set of backscattering points of coordinates  $(\theta, \varphi, R)$  in 3D space, where  $R$  is the range (or the radar-to-point separation distance). By defining  $d_\theta$  and  $d_\varphi$  as, respectively, the elevation and azimuthal steps used for the beamscanning, the 3D spatial resolution of the radar image is defined by the volume  $v_{res}$  of a so-called voxel as follows:

$$v_{res}(R, d) = \left(2R^2 + \frac{d^2}{6}\right) d d_\varphi \sin \frac{d_\theta}{2} \quad (1)$$

The geometrical representation of one voxel and spatial resolution  $v_{res}$  in the 3D radar image are illustrated on Fig. 1. Following Eq.(1), the volume  $v_{res}$  increases as the range  $R$  increases in a fixed beamscanning direction. Moreover, the wider the modulation bandwidth  $B$ , the smaller the depth resolution  $d$  and consequently, the smaller the voxel volume  $v_{res}$  (Note that the definition of this volume does not explicitly take into account the radiation pattern of the Tx and Rx radar antennas).

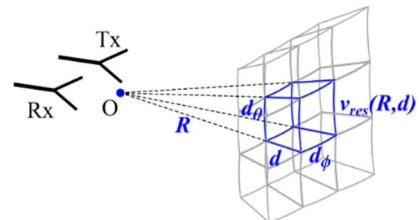


Fig. 1. Geometrical illustration of the voxel (in blue) and its volume  $v_{res}$  extracted from the beamscanning of a monostatic FM-CW radar located at point O.

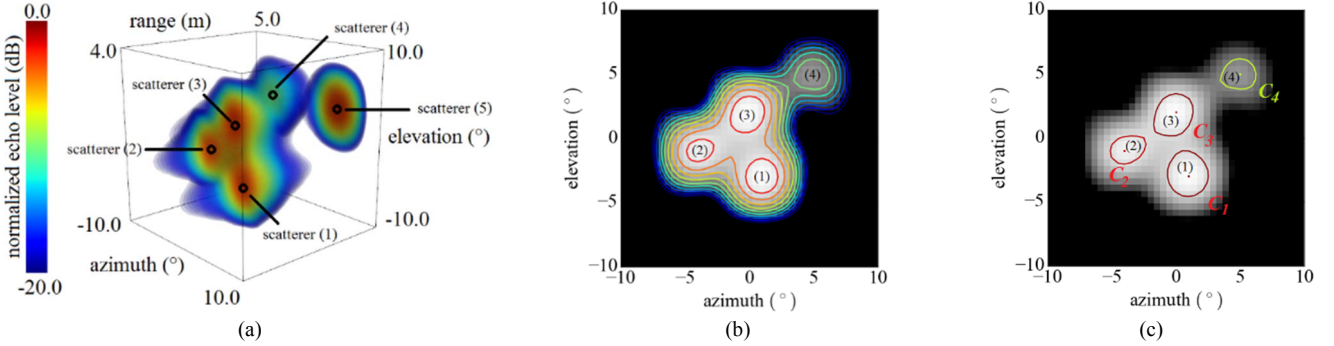


Fig. 2. (a) Simulated 3D radar image obtained from 5 omnidirectional scattering points distributed in the far-field region. The surfaces on which echo levels are the same are called *isosurfaces* [8] and are displayed on the image; (b) 2D radar image extracted from Fig. 2(a) at the range of 4.05m with its so-called *isolines*. Along an isoline, the echo level is the same: along the blue isoline, the echo level is of -20.0dB, while along the red isoline, this level is of 0.0dB; (c) The set  $\mathcal{C} = \mathcal{C}_1 \cup \mathcal{C}_2 \cup \mathcal{C}_3 \cup \mathcal{C}_4$  of the four isolines  $\mathcal{C}_k$  ( $k = 1, 2, 3, 4$ ) which enclose (or isolate) the scattering points detected at 4.05 m from the radar. This set  $\mathcal{C}$  of isolines have been derived from applying the proposed segmentation algorithm.

### B. Novel segmentation technique for 3D radar images

For illustration purpose, Fig. 2(a) displays with isosurfaces [8] the simulated 3D radar image obtained from 5 omnidirectional scattering points distributed in the far-field region. Table 1 gives details (location and radar-cross section) about these scattering points. The objective is to detect the 5 scattering points from the appropriate segmentation of the 3D radar image of Fig. 2(a).

The technique proposed here is to segment the image with *isolines*, that is, lines along which echo levels are the same. Isolines are expected to enclose each scattering point contained in the radar image. They are displayed on Fig. 2(b) at a distance of 4.05m from the radar, and are computed from applying the classical marching cubes algorithm [9]. We observe that isolines along which the echo levels are low enclose many scattering points. Moreover, isolines along which the echo levels are high (around 0dB) may enclose a unique scattering point (such as, the red isolines in Fig. 2(b), which individually enclose the scattering points #1, #2 and #3). However, scattering points with low radar cross section, such as, scattering point #4, may not be detected by such high iso-echo lines. In order to systematically enclose by isolines all scattering points, regardless of their radar cross-section and/or position, the following segmentation algorithm is applied:

\* *Step 1*: For each plane in azimuth/elevation, isolines with different echo levels are generated, starting from an initial echo threshold;

\* *Step 2*: The number of scattering points which are enclosed by all isolines is determined. We assume here that a scattering point brings one echo peak (or local maximum) in the region enclosed by an isoline;

\* *Step 3*: If more than one echo peak is detected for a given isoline, then the echo level defining this line is increased until only one peak is detected.

Fig. 2(c) displays the isolines computed from this segmentation algorithm. We note that each scattering point is now enclosed by an isoline. For example, scattering points #2 and #4 are isolated with isolines along which echo level is of -2.3dB and -9.6dB, respectively. The scattering points isolated by the

segmentation algorithm are detected in the azimuth/elevation plane, which defines a so-called *surface domain*  $S$ . We define  $\mathcal{C} = \mathcal{C}_1 \cup \mathcal{C}_2 \dots \cup \mathcal{C}_N$  the set of  $N$  isolines that delimits this surface domain. Voxels (defined in section II.A) inside  $\mathcal{C}$  constitute the valuable information about scatterers in the illuminated scene. This information will be used differently, depending on the targeted application, as it will be detailed in section III.

Table 1. Position and radar cross section of 5 scattering points in the illuminated scene.

Scattering points coordinates and Radar Cross Section				
Point	$R_k$ (m)	$\theta_k$ (°)	$\varphi_k$ (°)	Radar Cross Section (m <sup>2</sup> )
#1	4.05	1.0	-3.0	1.0
#2	4.05	-1.0	-4.0	0.9
#3	4.05	2.0	0.0	1.0
#4	4.05	5.0	5.0	0.4
#5	4.20	3.0	6.0	1.0

## III. REMOTE SENSING APPLICATIONS OF ISOLINES

### A. Estimation of the grape yield in precision viticulture

The proposed segmentation algorithm based on the computation of isolines is applied here to the remote estimation of the grape yield from ground-based FMCW radars as proximal sensors. The main principle and results are detailed in [5]. We consider here a set of scatterers that are generated by a 3D beamscanning of vine plants with a ground-based FM-CW radar. As explained in section II.B, each scatterer is delimited by an isoline from a set  $\mathcal{C}$  of isolines. Fig. 3(a) shows the  $k^{th}$  isoline  $\mathcal{C}_k$  from the set  $\mathcal{C}$  of isolines which encloses voxels (see section II.A). To estimate the grape yield, we must determine the contribution of each scatterer to the mass of grapes in the illuminated scene. For this purpose, parameters defined inside the set  $\mathcal{C}$  of isolines associated with each scatterer are calculated. These parameters could be, for example: the echo peak  $e_{max}(\mathcal{C})$ , the echo mean value  $e_{mean}(\mathcal{C})$ , the echo

standard deviation  $e_{std}(\mathcal{C})$  in domain  $S$ , etc. We assume that  $\mathcal{N}$  scatterers are segmented from the 3D radar data set. We define  $U_k$  as the set of parameters calculated inside the  $k^{th}$  isoline  $\mathcal{C}_k$  from the set  $\mathcal{C}$  of isolines, such as  $U_k = \{e_{max}(\mathcal{C}_k), e_{mean}(\mathcal{C}_k), e_{std}(\mathcal{C}_k), etc.\dots\}$ . We assume finally that the statistical estimator of the grape yield, denoted  $E$ , depends only on  $U_k$ , as illustrated in Fig. 3(b). Results of these estimations based on magnitude and polarimetric analysis of radar echoes are summarized in Table 2 for various carrier frequencies  $f_c$  and modulation bandwidths  $B$ . We obtain very encouraging results with an error on the estimated mass of grapes less than 1% at 122GHz.

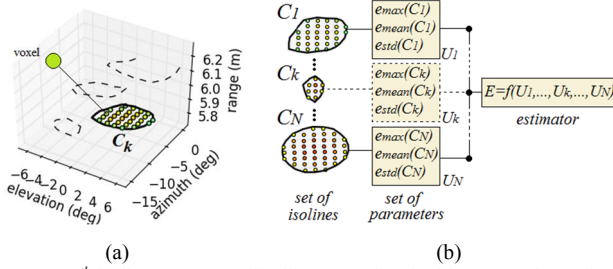


Fig. 3. (a)  $k^{th}$  isoline  $\mathcal{C}_k$  set  $\mathcal{C}$  of isolines associated with a scattering point and its parameters  $e_{max}(\mathcal{C})$ ,  $e_{mean}(\mathcal{C})$  and  $e_{std}(\mathcal{C})$ ; (b) Graphical representation of the grape yield estimator  $E$ . The estimator is built from the set of parameters  $U$  defined inside each set  $\mathcal{C}$  of computed isolines.

Table 2. Estimation results from different grape yields at 24GHz, 77GHz and 122GHz.

	24 GHz	77 GHz	122 GHz
$f_c$	24 GHz	77 GHz	122 GHz
$B$	2 GHz	3 GHz	6.8 GHz
estimation	polarimetric	magnitude	magnitude
harvested mass	48.1 kg	48.1 kg	31.4 kg
estimated mass	48.6 kg	51.9 kg	31.1 kg
error	1.1 %	7.3 %	0.9 %

### B. Monitoring apple trees in orchards

Another application of isolines consists of analysing the numbers of electromagnetic scatterers in the illuminated scene and calculating their surface  $s(\mathcal{C})$  for monitoring, e.g., a scene that changes over the time. In this example, three apple trees were monitored in an orchard from March to August 2017 in order to determine key dates for spraying and thinning apples. Each apple tree is illuminated with a 24GHz ground based FM-CW radar with a 2GHz modulation bandwidth. The distance between the radar and the apple trees is around 2m. The beamwidth of the Tx antenna is  $8^\circ$ . The resulting 3D radar data contain scattering points that are segmented according to the method described in section II.B. Derived isolines of these scatterers are displayed on Fig. 4(a) and 4(b) for an apple tree measured respectively in March and July 2017. Pictures of the apple tree are also displayed in Fig. 4(c) and 4(d). We observe that scatterers are numerous with small surfaces in July, whereas they are less numerous with larger surfaces in March. This phenomenon is explained by the development of leaves and small apples that generates the *fragmentation* or inversely, the *condensation* of the set of isolines.

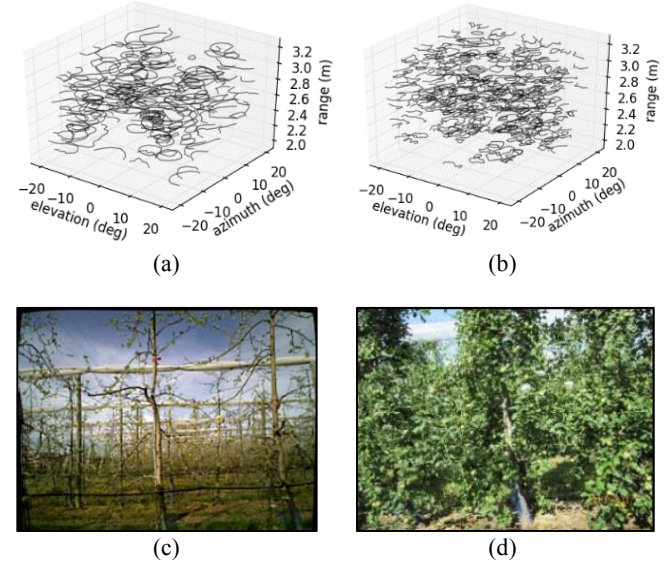


Fig. 4. Set of isolines in 3D radar images of an apple tree illuminated in (a) March and (b) July 2017. Pictures of the illuminated scene are displayed in (c) March and (d) July.

Table 3. Number of scatterers and average surface of segmented scatterers for three apple trees during different stages of development.

apple tree #1	March	April	July	August
$\mathcal{N}$	135	182	231	169
$s_{mean}$ (pixels $^2$ )	23	16	11	18
apple tree #2	March	April	July	August
$\mathcal{N}$	160	196	227	171
$s_{mean}$ (pixels $^2$ )	17	15	11	17
apple tree #3	March	April	July	August
$\mathcal{N}$	141	156	240	164
$s_{mean}$ (pixels $^2$ )	16	16	10	19

To quantify this fragmentation or condensation of isolines, or in other words, the density of isolines in the 3D radar images, we define  $\mathcal{N}$  as the total number of isoline set in the illuminated scene. The average surface delimited by sets of isolines is defined by:

$$s_{mean} = \frac{1}{\mathcal{N}} \sum_{k=1}^{\mathcal{N}} s(\mathcal{C}_k) \quad (2)$$

where  $\frac{1}{\mathcal{N}}$  represents the density of isoline sets in the 3D radar image.  $\mathcal{N}$  and  $s_{mean}$  are reported in Table 3 for the three apple trees illuminated from March to August. From March to July, since  $\mathcal{N}$  increases, while  $s_{mean}$  decreases, the fragmentation of isolines due to the developments of small electromagnetic scatterers, such as leaves and apples. From July to August, leaves stop to grow while the size of apples size continues to increase. Apples gather together to create larger scatterers. Consequently, the condensation of isolines appears and the value of  $\mathcal{N}$  decreases, while  $s_{mean}$  increases (and consequently, the density of isolines decreases). This phenomenon of fragmentation and condensation of isolines

might be useful for monitoring plant and tree developments, and may be eventually correlated with well-known biological parameters, such as the Leaf Area Index.

### C. Monitoring vine plants in vineyards

Instead of analysing isolines in one polarization coupling, we may consider several polarization couplings. We define the set of isolines  $\mathcal{C}^p$  that is generated in polarization coupling  $p$ . For example, the notation  $\mathcal{C}^{VH}$  denotes the set of isolines from a 3D radar data set generated with a vertically polarized radar Tx-antenna and horizontally polarized radar Rx-antenna. The beamwidth of the Tx antenna is  $8^\circ$ .

Such concept is illustrated in Fig. 5 where the sets  $\mathcal{C}^{VV}$  and  $\mathcal{C}^{VH}$  for five beamscanned vine plants have been generated in (a) May, (b) June and (c) July at 24GHz. The sets  $\mathcal{C}^{VV}$  and  $\mathcal{C}^{VH}$  are respectively in black and green colors. As expected, the fragmentation of isoline sets is clearly visible on both polarization couplings from May to July. This phenomenon is correlated to the development of foliage, as seen in pictures in Fig. 5. More results are reported in Table 4, where the number of isoline sets and the average surface delimited by these sets are estimated from May to September for  $p=VV$  and  $p=VH$ . We observe that the fragmentation stops in August. From August to September, the condensation is observed. It may originate from the growing development of grapes that creates larger electromagnetic scatterers, while the foliage development has slowed down (similarly to apple trees, see section III.B). Note that the condensation is more sensitive in cross-polarization coupling than in co-polarization coupling ( $S_{mean}$  increases by 3 pixels $^2$  and 8 pixels $^2$  respectively for VV and VH).

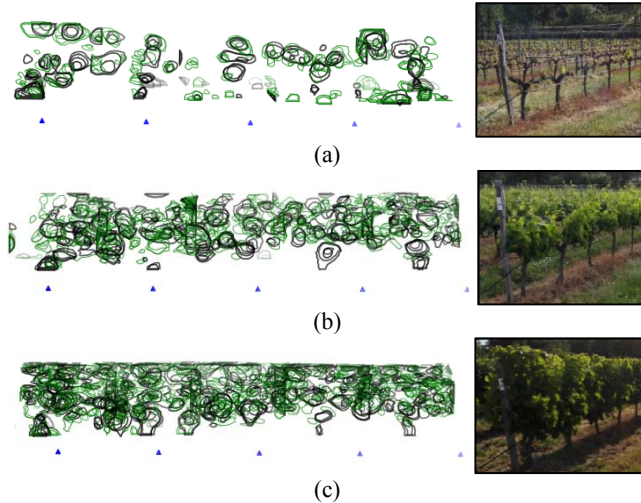


Fig. 5. Pictures (right) and sets of computed isolines in 3D radar images (left) of five vine plants illuminated in (a) May, (b) June and (c) July. The sets  $\mathcal{C}^{VV}$  and  $\mathcal{C}^{VH}$  are displayed respectively in black and green colors. Blue triangles represent the positions of the radar for each beamscanning.

### IV. CONCLUSION

We have reported a new technique for detecting and remotely analysis electromagnetic scatterers embedded in a scene from 3D radar images. Isolines have been advantageously

computed for detecting and remotely analysing these scatterers. Application to precision agriculture have been discussed. It is shown that isolines might be useful to correlate estimators from scatterers to biological parameters, such as the Leaf Area Index or the pruning weight.

Table 4. Number of scatterers and average surface of segmented scatterers for the five vine plants during different stages of development.

date <sup>a</sup>	$\mathcal{N}^{VV}$	$S_{mean}^{VV}$ <sup>b</sup>	$\mathcal{N}^{VH}$	$S_{mean}^{VH}$ <sup>b</sup>
04/05	138	22	185	15
01/06	311	19	411	13
06/07	531	17	656	12
03/08	524	14	642	7
23/08	423	17	571	12
13/09	447	17	562	15

<sup>a</sup> dd/mm of year 2017 <sup>b</sup> in pixels $^2$

### ACKNOWLEDGMENTS

The authors would like to thank T.Véronèse and Ovalie-Innovation for their financial support, and E.Serrano and the staff of IFV Sud-Ouest (*Institut Français de la Vigne et du Vin*) for their expertise and the authorized access of the IFV Sud-Ouest vineyards.

### REFERENCES

- [1] E. Ozturk, D. Genschow, U. Yodprasit, B. Yilmaz, D. Kissinger, W. Debski and W. Winkler, "Measuring Target Range and Velocity: Developments in Chip, Antenna, and Packaging Technologies for 60-GHz and 122-GHz Industrial Radars", in IEEE Microwave Magazine, vol. 18, no. 7, pp. 26-39, Nov. 2017
- [2] S. Thomas, C. Bredendiek, T. Jaeschke, F. Vogelsang, et N. Pohl, « A compact, energy-efficient 240 GHz FMCW radar sensor with high modulation bandwidth », in 2016 German Microwave Conference (GeMiC), 2016, p. 397-400
- [3] H. J. Ng, M. Kucharski and D. Kissinger, "Scalable sensor platform with multi-purpose fully-differential 61 and 122 GHz transceivers for MIMO radar applications," 2016 IEEE Bipolar/BiCMOS Circuits and Technology Meeting (BCTM), New Brunswick, NJ, 2016, pp. 170-173.
- [4] P. Hügler, F. Roos, M. Schartel, M. Geiger and C. Waldschmidt, "Radar Taking Off: New Capabilities for UAVs," in IEEE Microwave Magazine, vol. 19, no. 7, pp. 43-53, Nov.-Dec. 2018
- [5] D. Henry, H. Aubert and T. Véronèse, "Proximal Radar Sensors for Precision Viticulture," in IEEE Transactions on Geoscience and Remote Sensing, in press. [Online]. Available (early and open access): <https://ieeexplore.ieee.org/document/8631170>.
- [6] A. Broquetas, A. Aguasca, A. Martinez and R. Tomás, "Structural Health Monitoring with 94 Ghz Radar," IGARSS 2018 - 2018 IEEE International Geoscience and Remote Sensing Symposium, Valencia, 2018, pp. 7982-7985.
- [7] D. Henry, H. Aubert, E. Ricard, D. Hazard, and M. Lihoreau, "Automated Monitoring of Livestock Behavior Using Frequency-Modulated Continuous-Wave Radars", Progress In Electromagnetics Research M, Vol. 69, 151-160, 2018.
- [8] P. Ramachandran and G. Varoquaux, " Mayavi: 3D Visualization of Scientific Data", Comput. Sci. Eng., vol. 13, no 2, p. 40-51, Mar. 2011.
- [9] Scikit-Image: Image Processing SciKit (Toolbox for SciPy). Accessed: Mar. 20, 2018. [Online]. Available: <http://github.com/scikitimage>